quasi-uniform spin modes, in contrast, are more "internal" to their respective textures and were not appreciably affected by roughness because they did not exhibit energy densities highly localized at the surface, as shown in fig. S8 (*8*).

The direct correlation of spin dynamics with complementary information in the magnetization hysteresis curves typically has been an experimental challenge; most techniques yield high-quality, interpretable observations of one or the other. Thin-film polycrystalline permalloy provides another dramatic example of the capability of TMRS to report both on the equilibrium landscape and on the nonequilibrium response. Averaged torque spectra of the vortex gyrotropic mode in a 15-nm-thick, 2-μm-diameter permalloy disk [deposited onto a torque sensor, as described in (*28*)] are shown in Fig. 4C. The drop-outs of the resonance signal correlated with plateaus of reduced differential susceptibility and correspond to applied field ranges where the vortex core is strongly pinned by grain boundary–dominated magnetic disorder (*29*, *30*). Between these regions, the core could be driven to large amplitude gyration, generating strong resonance signals (*31*).

TMRS provides excellent coupling to small specimens, resulting in high spin sensitivities (*8*). The simplicity of the technique is owed to the recent development of multi-ultrahigh frequency lock-in instrumentation (*10*) and to the natural compatibility of RF transmission line actuators (*8*) with on-chip nanomechanical torque sensors. Straightforward processing to integrate samples onto sensors (*28*, *32*) opens TMRS to a wide variety of materials. The approach is fully broadband, is massively scalable through microfabrication, and has intriguing potential for low-frequency work where induction signals become very small, per Faraday's law. The amplitude of the TMRS torque is frequency-independent.

In addition to the capabilities of simultaneous monitoring of equilibrium net magnetization, detection of the transverse RF moment in TMRS opens the door to porting methods of pulse magnetic resonance to torque-detection platforms. Torque spectroscopy will find utility as a vehicle to explore phenomena in emerging spin-mechanical physics (*33*, *34*). Broadband TMRS forms a foundation for nanomagnetism lab-on-a-chip applications for highly sensitive, noninvasive, and rapid prototyping of individual mesoscopic elements, and it presents another functional method to create and read out dynamic spin-based devices.

REFERENCES AND NOTES

1. H. J. Mamin *et al.*, *Nano Lett.* **9**, 3020–3024 (2009).
2. D. Rugar *et al.*, *Nat. Nanotechnol.* **10**, 120–124 (2015).
3. J. A. Sidles *et al.*, *Rev. Mod. Phys.* **67**, 249–265 (1995).
4. D. Rugar *et al.*, *Science* **264**, 1560–1563 (1994).
5. Z. Zhang, P. C. Hammel, M. Midzor, M. L. Roukes, J. R. Childress, *Appl. Phys. Lett.* **73**, 2036 (1998).
6. G. Alzetta, E. Arimondo, C. Ascoli, A. Gozzini, *Nuovo Cim.* **52**, 392–402 (1967).
7. C. Ascoli *et al.*, *Appl. Phys. Lett.* **69**, 3920 (1996).
8. Supplementary materials are available on *Science* Online.
9. F. Bloch, W. W. Hansen, W. Packard, *Phys. Rev.* **70**, 474–485 (1946).
10. Zurich Instruments, Zurich, Switzerland; model UHF lock-in amplifier with MF and MOD options (www.zhinst.com).
11. L. D. Landau, E. M. Lifshitz, . *Phys. Zeitschr. Sow.* **8**, 153 (1935).
12. J. Griffiths, *Nature* **158**, 670–671 (1946).
13. T. Kikkawa *et al.*, *Phys. Rev. Lett.* **110**, 067207 (2013).
14. B. Heinrich *et al.*, *Phys. Rev. Lett.* **107**, 066604 (2011).
15. J. Flipse, F. L. Bakker, A. Slachter, F. K. Dejene, B. J. van Wees, *Nat. Nanotechnol.* **7**, 166–168 (2012).
16. C. Hahn *et al.*, *Phys. Rev. Lett.* **111**, 217204 (2013).
17. A. A. Serga, A. V. Chumak, B. Hillebrands, *J. Phys. D Appl. Phys.* **43**, 264002 (2010).
18. C. Kittel, *Phys. Rev.* **71**, 270–271 (1947).
19. Shin Etsu Chemical Corporation, Tokyo, Lot Number SEW-3571 (www.rare-earth.jp).
20. R. P. Cowburn, D. K. Koltsov, A. O. Adeyeye, M. E. Welland, D. M. Tricker, *Phys. Rev. Lett.* **83**, 1042–1045 (1999).
21. M. Rahm *et al.*, *Appl. Phys. Lett.* **82**, 4110 (2003).
22. F. Guo, L. M. Belova, R. D. McMichael, *Phys. Rev. Lett.* **110**, 017601 (2013).
23. G. Woltersdorf, C. H. Back, *Phys. Rev. Lett.* **99**, 227207 (2007).
24. Y. Nozaki *et al.*, *Appl. Phys. Lett.* **91**, 082510 (2007).
25. S. Wintz *et al.*, *Phys. Rev. Lett.* **110**, 177201 (2013).
26. J. P. Park, P. Eames, D. M. Engebretson, J. Berezovsky, P. A. Crowell, *Phys. Rev. B* **67**, 020403 (2003).
27. O. V. Sukhostavets *et al.*, *Phys. Rev. Lett.* **111**, 247601 (2013).
28. Z. Diao *et al.*, *J. Vac. Sci. Technol. B* **31**, 051805 (2013).
29. T. Uhlig *et al.*, *Phys. Rev. Lett.* **95**, 237205 (2005).
30. J. A. J. Burgess *et al.*, *Science* **339**, 1051–1054 (2013).
31. T. Y. Chen, Magnetic vortex dynamics: Non-linear dynamics, pinning mechanisms, and dimensionality crossover, Ph.D. thesis, University of Minnesota (2012).
32. J. E. Losby *et al.*, *J. Appl. Phys.* **111**, 07D305 (2012).
33. S.-H. Lim *et al.*, *Europhys. Lett.* **105**, 37009 (2014).
34. S. T. B. Goennenwein, G. E. W. Bauer, S. Maekawa, Eds., *Solid State Commun.* **198** (2014). Special Issue: Spin Mechanics.

ACKNOWLEDGMENTS

The authors very gratefully acknowledge support from Natural Sciences and Engineering Research Council Canada (RGPIN 170827-2010, RGPIN 04239, and RGPIN 2014-04796), Canada Research Chairs (950206567), Alberta Innovates Technology Futures (iCiNano), National Institute for Nanotechnology (NINT A1-004906), Canada Foundation for Innovation (20314), Manitoba Research and Innovation Fund, and Canadian Microelectronics Corp. The nanomechanical torque sensors were fabricated at the University of Alberta NanoFab and NINT. Electron diffraction was performed by P. Li at the NINT microscopy center. D. Fortin assisted in the design and rendering of Fig. 1A. We thank J. P. Davis and R. Lockwood for critical reading of the manuscript, R. E. Wasilyshen for useful conversations, and anonymous referees for constructive suggestions. The data described in the paper are available upon request.

SUPPLEMENTARY MATERIALS

www.sciencemag.org/content/350/6262/798/suppl/DC1
Materials and Methods
Supplementary Text
Figs. S1 to S8
References (*35*–*50*)

16 August 2015; accepted 9 October 2015
10.1126/science.aad2449

GAMMA-RAY ASTRONOMY

An extremely bright gamma-ray pulsar in the Large Magellanic Cloud

The Fermi LAT Collaboration*†

Pulsars are rapidly spinning, highly magnetized neutron stars, created in the gravitational collapse of massive stars. We report the detection of pulsed giga–electron volt gamma rays from the young pulsar PSR J0540–6919 in the Large Magellanic Cloud, a satellite galaxy of the Milky Way. This is the first gamma-ray pulsar detected in another galaxy. It has the most luminous pulsed gamma-ray emission yet observed, exceeding the Crab pulsar's by a factor of 20. PSR J0540–6919 presents an extreme test case for understanding the structure and evolution of neutron star magnetospheres.

The first pulsar was discovered in 1967 as a puzzling celestial source of periodic radio pulses. Nearly 2500 pulsars have since been detected, mostly in the Milky Way but also in other nearby galaxies, and their characteristic pulsed emission has been observed across the electromagnetic spectrum. The energy source for emission from pulsars is the rotation of a magnetized neutron star. The mechanism is radiation by particles accelerated by intense electric fields in the neutron star magnetosphere. The pulsar spins with period P, and the observed rate at which it slows down, $\frac{dP}{dt} = \dot{P}$, sets the scale of the power reservoir for particle acceleration and emission processes. Spin-down power is $\dot{E} = 4\pi^2 I\dot{P}/P^3$, where I denotes the neutron star moment of inertia, taken to be 10^{45} g cm^2 (*1*), which roughly corresponds to a solid sphere of 10 km radius and the mass of the Sun.

The Large Area Telescope (LAT), an imaging instrument on the Fermi satellite sensitive to gamma rays with energies of 20 MeV to 300 GeV (*2*), has detected gamma-ray pulsations from more than 160 pulsars (*3*, *4*). Gamma-ray pulsars have $\dot{E} > 10^{33}$ erg s^{-1}, and a large fraction (>30% in many cases) of their spin-down power is converted into gamma-ray luminosity L_γ. In contrast, radio emission represents a negligible fraction of the total energy output (*3*). Gamma-ray observations thus probe the sites and processes of particle acceleration and radiation in pulsars. Candidate emission regions range across the magnetosphere out to the "light cylinder," where co-rotation with the neutron star would reach the speed of light (*5*–*7*). In these regions, curvature or synchrotron radiation from accelerated electrons initiates electromagnetic cascades by interacting with the strong magnetic field or with ambient photons; the electron-positron pairs

*All authors with their affiliations appear at the end of this paper. †Corresponding author. E-mail: pierrick.martin@irap.omp.eu (P.M.); lucas.guillemot@cnrs-orleans.fr (L.G.); francis.e.marshall@nasa.gov (F.M.)

produced are accelerated and radiate in turn, giving rise to further pairs. Emission may also originate in the pulsar's plasma wind, beyond the light cylinder (*8*).

Discriminating between emission scenarios requires spectra and light curves in various wavebands for pulsars with different ages, magnetic field strengths, and viewing geometries. Few pulsars younger than several thousand years are known. The pulsar in the Crab supernova remnant is the best studied and was the most powerful known in pulsed gamma rays (*9*). The Crab pulsar has $\dot{E} = 4.5 \times 10^{38}$ erg s^{-1}. Only one known pulsar has a larger spin-down power—PSR J0537–6910, with $\dot{E} = 4.9 \times 10^{38}$ erg s^{-1}—whereas PSR J0540–6919, only 16 arc min away, has the third highest, $\dot{E} = 1.5 \times 10^{38}$ erg s^{-1}. Both of the latter are located in the Large Magellanic Cloud (LMC), a satellite galaxy of the Milky Way at a distance $d \sim 50$ kpc (*10*). PSR J0537–6910 is a 16-ms pulsar associated with the ~5000-year-old supernova remnant LHA 120-N 157B (*11*, *12*), whereas PSR J0540–6919 is a 50-ms pulsar associated with the ~1140-year-old supernova remnant SNR 0540-69.3 (*13*–*15*). Although these two pulsars are of comparable age and energetics, their gamma-ray behavior appears to be markedly different. This paper reports the detection of gamma-ray pulsations from PSR J0540–6919 and an upper limit on gamma-ray pulsations from PSR J0537–6910.

Fermi-LAT predominantly operates in all-sky survey mode; hence, the LMC has been observed regularly since launch. Gamma-ray emission from the LMC is particularly prominent near the Tarantula nebula (30 Doradus) (*16*), a very active star-forming region that hosts extremely massive stars (*17*, *18*). PSR J0537–6910 and PSR J0540–6919 lie in this area, but until now, neither could be identified as discrete gamma-ray sources. Now, more than six times more data are available as compared with the earlier Fermi-LAT study (*16*), and the recent revision of LAT event reconstruction, called Pass 8, substantially enhanced the sensitivity of LAT data analyses (*19*). We thus revisited the gamma-ray emission from the LMC, and the 30 Doradus region in particular.

We analyzed Pass 8 events from 75 months of Fermi-LAT all-sky survey observations (*20*). The gamma-ray emission from the LMC is shown in Fig. 1, after subtracting fitted models of the Galactic foreground emission, an isotropic background, and pointlike sources outside the LMC. The improved angular resolution with increasing gamma-ray energy makes two pointlike sources coincident with the pulsars stand out above 2 GeV.

The source coincident with PSR J0540–6919 is detected with a statistical significance of 17σ. Its photon spectrum is well described by a power law with exponential cutoff, which is typical of gamma-ray pulsars (*3*). To search for pulsations, we built a rotation ephemeris using Rossi X-ray Timing Explorer (RXTE) (*21*) observations recorded between modified Julian day 54602 (16 May 2008) and 55898 (3 December 2011), shortly before the end of the RXTE mission (table S1). We phase-folded the gamma-ray data from the first 3.5 years of the *Fermi* mission corresponding to the ephemeris. We used the LMC emission model to assign each photon the probability that it originated from PSR J0540–6919, on the basis of reconstructed positions and energies and the instrument response functions (*22*). The probability-weighted $E > 100$ MeV gamma-ray pulse profile for probabilities >0.1 is shown in Fig. 2. The weighted H test parameter (*22*, *23*) is 63.5, corresponding to a significance of 6.8σ, making this the first extragalactic gamma-ray pulsar.

Time-averaged gamma-ray emission from the source coincident with PSR J0537–6910 is detected with significance 11σ. Its spectrum is consistent with a simple power law with photon index 2.1 ± 0.1 extending to >50 GeV without evidence for a cutoff. A weighted phase-fold of the LAT data-based on an RXTE ephemeris limited any pulsed emission to significance <1σ (table S2). The 95% confidence level upper limit on the 0.1 to 10 GeV pulsed luminosity for this pulsar is 1.9×10^{35} erg s^{-1}. This and the lack of a spectral cutoff suggest that strongly pulsed emission is at most a small fraction of the total signal from the source. The gamma-ray signal may instead result from the superposition of weakly modulated pulsar emission and radiation from the pulsar wind nebula and the supernova remnant, in unknown proportions.

The x-ray pulse profile for PSR J0540–6919 is also shown in Fig. 2, obtained by integrating all the RXTE data used to build the timing solution. The profile matches previous results (*24*). We evaluated the optical light curve using the RXTE ephemeris to fold data from the Iqueye photometer mounted on the European Southern Observatory 3.6-m New Technology Telescope (NTT) in January and December 2009 (*25*). We also show a radio profile formed from the sum of 18 bright giant pulses recorded at the Parkes telescope at 1.4 GHz in August 2003 (*26*). Emission components from radio to gamma rays are aligned, but the shape of the pulse varies over the different

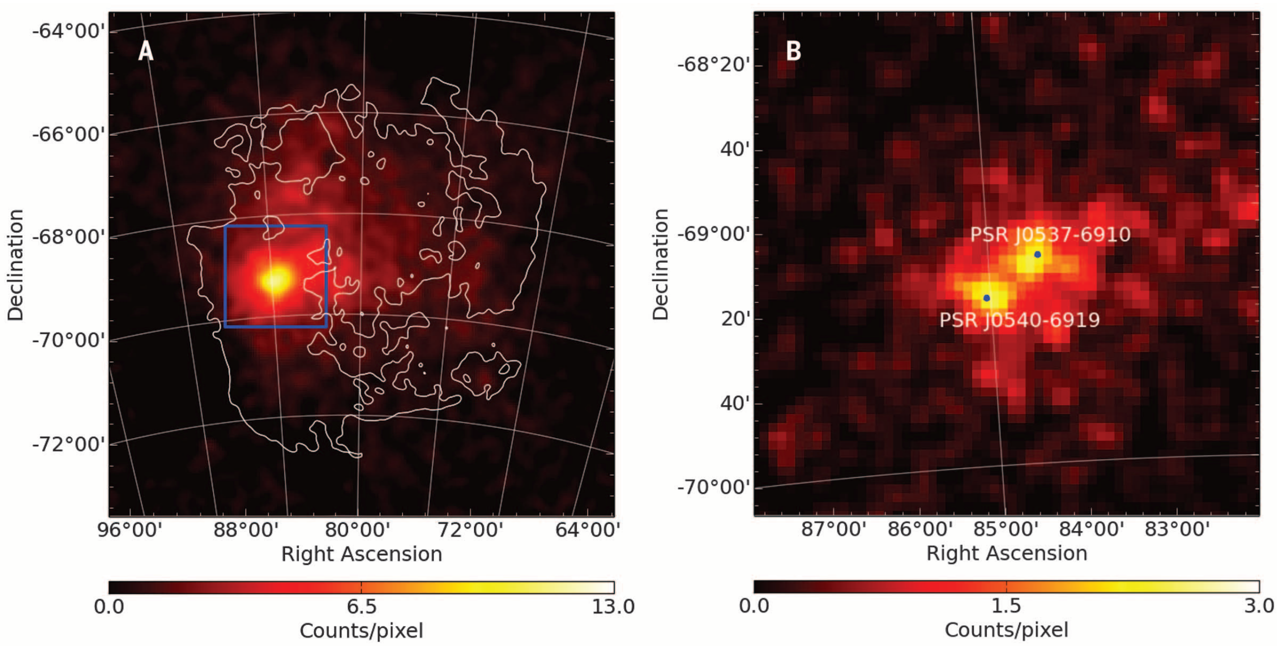

Fig. 1. Sky maps of the LMC. (**A**) 0.2 to 200 GeV gamma-ray emission in a 10° by 10° region encompassing the LMC. The map was smoothed by using a Gaussian kernel with σ = 0.2°. Emission is strongest around 30 Doradus (approximately delimited by the blue box) but also fills much of the galaxy. Contours show the atomic gas distribution. (**B**) 2 to 200 GeV gamma-ray emission in a 2° by 2° region around 30 Doradus. The map was smoothed by using a Gaussian kernel with σ = 0.1°. Better angular resolution at higher energies resolves two components coincident with PSR J0540–6919 and PSR J0537–6910, whose locations are indicated as blue dots. Both maps are given in J2000 equatorial coordinates.

bands. The radio profile exhibits two narrow peaks separated by $\Delta \sim 0.25$ in pulse phase. This double-peak pattern is still visible on top of a broader component in the optical profile. Structures in the x-ray and perhaps gamma-ray profiles are reminiscent of the double radio peaks separated by $\Delta \sim 0.25$, but both profiles are consistent with a single bump spanning the interval between the radio peaks. In outer-magnetosphere models, the pulse peak profiles are sensitive to the magnetic geometry. In the classical vacuum "outer gap" model (*5*), pulse separations as small as $\Delta = 0.25$ occur for high-$\dot{E}$, narrow-gap pulsars when the spin-axis viewing angle ζ is >80° and the magnetic inclination α is <30° (*27*). Models with partly resistive magnetospheres and emission extending beyond the light cylinder point to $\zeta \approx 60°$ and $\alpha \approx 30°$, but differing resistivity prescriptions may allow larger ζ (*7*). For such geometry, the low-altitude classical radio emission would not be observable, leaving only the high-altitude giant pulse component.

The signal above the background estimate in Fig. 2 suggests a steady component of the gamma-ray emission from the direction of PSR J0540−6919. Likelihood analysis of the data in the off-pulse phase interval 0.3 to 0.8 shows a significant (~5σ) point source at the position of PSR J0540−6919. The spectrum is consistent with that of the full phase interval but may be almost as well described by a single power law (fig. S1). We cannot currently distinguish whether this represents an unpulsed magnetospheric component, emission from the associated pulsar wind nebula LHA 120-N 158A or from the surrounding supernova remnant SNR 0540-69.3, or residual emission from the LMC itself. Comparing with the flux in the on-pulse phase interval, we estimate that the pulsed component is ≈75% of the total. The choice of the off-pulse phase interval, hence the unpulsed flux estimate, is conservative because it clearly includes pulsed optical and x-ray emission (Fig. 2).

The phase-averaged spectrum of PSR J0540−6919 is shown in Fig. 3. The photon spectrum is well described by a power law with photon index 2.2 ± 0.1 and exponential cutoff at $E_{\mathrm{cut}} = 7.5 \pm 2.6$ GeV. This photon index follows the trend of increasing index with $\dot{E}$ described in (*3*). This correlation can be explained by stronger pair formation activity in high-$\dot{E}$ pulsars, reprocessing the radiation to lower energies and leading to steep radiating particle spectra. PSR J0540−6919 has the second largest magnetic field at the light cylinder of any gamma-ray pulsar known, after the Crab pulsar, with $B_{\mathrm{LC}} = 4\pi^2 (I\dot{P})^{1/2} (c^3 P^5)^{-1/2} = 3.62 \times 10^5$ G. Our E_{cut} measurement favors the trend of increasing cutoff energy as a function of B_{LC}, also noted in (*3*), suggesting emission originating from the outer magnetosphere of the neutron star.

The total phase-averaged luminosity of PSR J0540−6919 above 100 MeV is $L\gamma = 4\pi f_{\Omega} h d^2 = 7.6 \times 10^{36} (d/50\ \mathrm{kpc})^2$ erg s^{-1}, where $h = (2.6 \pm 0.3) \times 10^{-11}$ erg cm^{-2} s^{-1} is the energy flux, and the geometry-dependent beaming correction factor is $f_{\Omega} \sim 1$ for young pulsars with the most probable viewing angle of ~90° (*27*), which is consistent with the geometrical setting derived above. As stated above, ≈75% of the total luminosity is pulsed and may be safely attributed to the pulsar, 5.7×10^{36} erg s^{-1}. The systematic uncertainties in the spectrum and luminosity of the source due to the complete LMC emission model were found to be smaller than the statistical uncertainties (*28*). And whereas other pulsars' luminosities can be severely affected by distance uncertainties (for example, 25% for the Crab pulsar), for PSR J0540−6919, the distance to the LMC is known to 2% accuracy (*10*).

PSR J0540−6919 is often called the "Crab's twin" because they have similar magnetic field strengths, rotation rates, and ages, so a comparison is in order. The Crab pulse profile has two peaks, phase-aligned from the radio to the gamma-ray band, whereas PSR J0540−6919 has a broad gamma-ray pulse straddling the phase-range of the two narrow radio peaks, with structures in

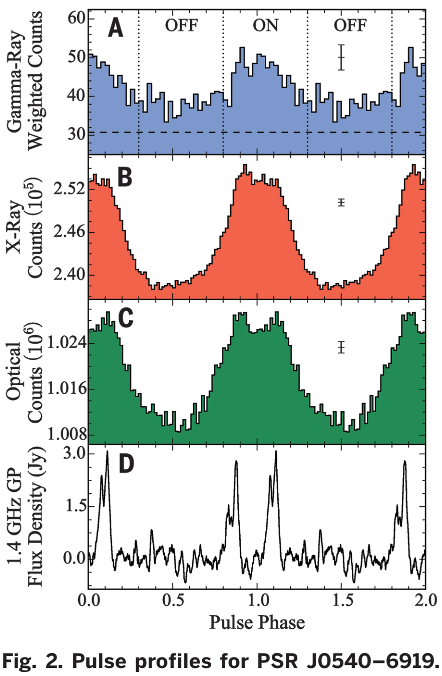

Fig. 2. Pulse profiles for PSR J0540−6919. (**A**) Probability-weighted LAT count profile. The horizontal dashed line approximates the background level. Vertical lines indicate the on- and off-pulse regions used for the LAT spectral analysis. (**B**) RXTE x-ray integrated count profile. (**C**) NTT optical count profile. (**D**) Parkes radio flux profile from summing 18 bright giant radio pulses at 1.4 GHz. Two complete cycles are shown. The error bars in the top three panels represent the median phase bin errors.

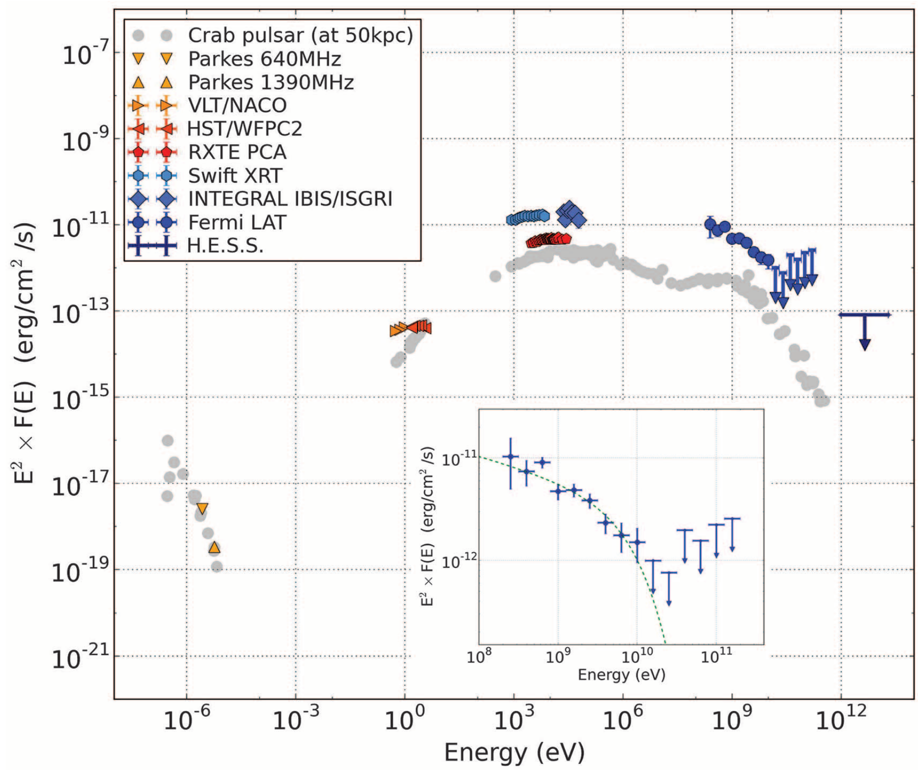

Fig. 3. Spectral energy distribution of PSR J0540−6919. Pulsed radio data are from (*26*, *39*). Extinction-corrected phase-averaged near-infrared and optical fluxes are from (*40*, *41*). X-ray fluxes are from (*24*), including pulsed RXTE data and total spectra for the pulsar and its nebula from Swift and INTEGRAL. Tera–electron volt upper limit is from (*33*). The LAT data points correspond to the phase-averaged emission, which includes an estimated 25% of unpulsed emission. Crab pulsar phase-averaged data rescaled to a 50 kpc distance are shown for comparison in light gray (*9*). (Inset) LAT data fit to a power law with an exponential cutoff.

the optical and x-ray reminiscent of the radio peaks. The similarity in their radio behavior is particularly meaningful because for both pulsars, the radio emission is dominated by so-called "giant pulses," sporadic radio bursts with submicrosecond durations and fluxes with a power-law distribution extending to $>10^3$ times the average value (*29*). In (*26*), it is suggested that the colocation of the giant pulses with high-energy emission occurs in pulsars with high magnetic fields at the light cylinder and very robust and extensive outer-magnetosphere pair production. Before this work, only six other pulsars showed giant pulse emission associated with strong optical, x-ray, or gamma-ray components (*30*). The discovery of gamma-ray emission from PSR J0540–6919 provides a new look at these rare sources.

PSR J0540–6919 and the Crab also share many spectral similarities, as illustrated in the radio-to–gamma ray spectral energy distribution (Fig. 3). With large powers in both pulsed x-rays and gamma rays and the absence of a strong high-energy cutoff, PSR J0540–6919 is similar to the Crab and unlike most middle-aged pulsars, where giga–electron volt gamma-ray power dominates. Both characteristics may originate from the higher pair densities that allow synchrotron self-Compton emission to dominate and produce higher-energy pulsations. It remains to be seen whether PSR J0540–6919 follows the Crab in exhibiting a high-energy tail of pulsed emission, extending far above E_{cut} and likely attributable to inverse Compton scattering (*31*, *32*). The source is currently undetected in tera–electron volt gamma rays (*33*) but may be in reach of future instruments, such as the Cherenkov Telescope Array.

Yet whereas the radio, optical, and x-ray luminosities of PSR J0540–6919 and the Crab are within a factor of ~2, PSR J0540–6919 is much brighter in gamma rays. Its isotropic pulsed gamma-ray luminosity is ~20 times more than the Crab pulsar's, $L_\gamma = 3.2 \times 10^{35}(d/2\ \mathrm{kpc})^2$ erg s^{-1} (*3*). PSR J0540–6919's pulsed luminosity remains larger than that of the Crab pulsar even when including their intense x-ray emission: Combining the 2 to 10 keV and 20 to 100 keV pulsed flux measurements from (*24*) gives an integrated luminosity for PSR J0540–6919 of $L_{X+\gamma} \sim 9.7 \times 10^{36}(d/50\ \mathrm{kpc})^2$ erg s^{-1}, whereas it becomes $L_{X+\gamma} \sim 2.4 \times 10^{36}$ $(d/2\ kpc)$ erg s^{-1} for the Crab (*34*).

The contrast with PSR J0537–6910 is even more striking: It has more than three times greater spin-down power, but its pulsed gamma-ray luminosity may be at least 30 times less than that of PSR J0540–6919. This confirms that L_γ values can vary by more than an order of magnitude for a given $\dot{E}$ range (*3*). Misestimated distances and deviations from $f_\Omega = 1$ can account for only part of this difference. The magnetic inclination may play a considerable role, beyond its effect on the beaming (*35*, *36*).

As mentioned above, the pulse profile of PSR J0540–6919 suggests a high viewing angle of $\zeta > 80°$ and a low magnetic inclination of $\alpha < 30°$. Fits to *Chandra* observations of the pulsar wind nebulae shapes of PSR J0540–6919 and PSR J0537–6910 indicate that both pulsars have similar viewing angles of $\zeta \sim 90°$ (*37*). In such conditions, the nondetection of radio emission from PSR J0537–6910 implies either a high magnetic inclination and a radio luminosity at most half that of PSR J0540–6919, or a misaligned radio beam, hence a low magnetic inclination similar to PSR J0540–6919 (*38*). The former case would confirm the role of the magnetic inclination in the observed dispersion of L_γ; the latter case would mean that the large difference in pulsed luminosity between both pulsars does not stem from different geometries. Alternatively, the nondetection of pulsations from PSR J0537–6910 may imply a weakly modulated gamma-ray light curve. The "outer gap" model predicts such flat pulse profiles for $\zeta = 90°$, $\alpha = 15°$, and a narrow gap (*27*), a geometry quite similar to that inferred for PSR J0540–6919. Very similar ages, energetics, and geometries for PSR J0540–6919 and PSR J0537–6910 would therefore result in remarkable emission differences.

Our gamma-ray measurements of PSR J0540–6919 and PSR J0537–6910 offer a new look at the high-altitude accelerators in the magnetospheres of rare very young pulsars. They also have profound implications for our understanding of the high-energy emission from the LMC: ≈60% of the GeV flux density previously attributed to the 30 Doradus nebula (*16*) is now seen to be emission from PSR J0540–6919. With an additional ≈25% attributable to the source coincident with PSR J0537–6910, only a small fraction of the signal may originate in cosmic rays in 30 Doradus. This calls for further investigation of the relation between star-forming regions and the origin and transport of cosmic rays.

REFERENCES AND NOTES

1. D. R. Lorimer, M. Kramer, *Handbook of Pulsar Astronomy* (Cambridge Univ. Press, Cambridge, 2004).
2. W. B. Atwood *et al*., *Astrophys. J.* **697**, 1071–1102 (2009).
3. A. A. Abdo *et al*., *Astrophys. J.* **208** (suppl.), 17 (2013).
4. The Fermi/LAT Collaboration, https://confluence.slac.stanford.edu/display/GLAMCOG/Public+List+of+LAT-Detected+Gamma-Ray+Pulsars (2015).
5. K. S. Cheng, C. Ho, M. Ruderman, *Astrophys. J.* **300**, 500 (1986).
6. A. G. Muslimov, A. K. Harding, *Astrophys. J.* **606**, 1143–1153 (2004).
7. C. Kalapotharakos, A. K. Harding, D. Kazanas, *Astrophys. J.* **793**, 97 (2014).
8. J. Pétri, *Mon. Not. R. Astron. Soc.* **412**, 1870–1880 (2011).
9. R. Bühler, R. Blandford, *Rep. Prog. Phys.* **77**, 066901 (2014).
10. G. Pietrzyński *et al*., *Nature* **495**, 76–79 (2013).
11. F. E. Marshall, E. V. Gotthelf, W. Zhang, J. Middleditch, Q. D. Wang, *Astrophys. J.* **499**, L179–L182 (1998).
12. Y. Chen *et al*., *Astrophys. J.* **651**, 237–249 (2006).
13. F. D. Seward, F. R. Harnden Jr., D. J. Helfand, *Astrophys. J.* **287**, L19 (1984).
14. B. J. Williams *et al*., *Astrophys. J.* **687**, 1054–1069 (2008).
15. T. Brantseg, R. L. McEntaffer, L. M. Bozzetto, M. Filipovic, N. Grieves, *Astrophys. J.* **780**, 50 (2014).
16. A. A. Abdo *et al*., *Astron. Astrophys.* **512**, A7 (2010).
17. P. A. Crowther *et al*., *Mon. Not. R. Astron. Soc.* **408**, 731–751 (2010).
18. N. R. Walborn *et al*., *Astron. Astrophys.* **564**, A40 (2014).
19. W. Atwood *et al*., 2012 Fermi Symposium proceedings—eConf C121028, http://arxiv.org/abs/1303.3514 (2013).
20. Materials and methods are available as supplementary materials on *Science* Online.
21. H. V. Bradt, R. E. Rothschild, J. H. Swank, *Astron. Astrophys.* **97** (Supp.), 355 (1993).
22. M. Kerr, *Astrophys. J.* **732**, 38 (2011).
23. O. C. de Jager, B. C. Raubenheimer, J. W. H. Swanepoel, *Astron. Astrophys.* **221**, 180 (1989).
24. R. Campana *et al*., *Mon. Not. R. Astron. Soc.* **389**, 691–700 (2008).
25. S. Gradari *et al*., *Mon. Not. R. Astron. Soc.* **412**, 2689–2694 (2011).
26. S. Johnston, R. W. Romani, F. E. Marshall, W. Zhang, *Mon. Not. R. Astron. Soc.* **355**, 31–36 (2004).
27. R. W. Romani, K. P. Watters, *Astrophys. J.* **714**, 810–824 (2010).
28. Fermi-LAT collaboration, http://arxiv.org/abs/1509.06903 (2015).
29. J. M. Cordes, N. D. R. Bhat, T. H. Hankins, M. A. McLaughlin, J. Kern, *Astrophys. J.* **612**, 375–388 (2004).
30. A. V. Bilous, T. T. Pennucci, P. Demorest, S. M. Ransom, *Astrophys. J.* **803**, 83 (2015).
31. VERITAS Collaboration *et al*., *Science* **334**, 69–72 (2011).
32. M. Lyutikov, N. Otte, A. McCann, *Astrophys. J.* **754**, 33 (2012).
33. H.E.S.S. Collaboration, *Science* **347**, 406–412 (2015).
34. R. Willingale *et al*., *Astron. Astrophys.* **365**, L212–L217 (2001).
35. L. Zhang, K. S. Cheng, Z. J. Jiang, P. Leung, *Astrophys. J.* **604**, 317–327 (2004).
36. G. Brambilla, C. Kalapotharakos, A. K. Harding, D. Kazanas, *Astrophys. J.* **804**, 84 (2015).
37. C.-Y. Ng, R. W. Romani, *Astrophys. J.* **673**, 411–417 (2008).
38. F. Crawford, M. McLaughlin, S. Johnston, R. Romani, E. Sorrelgreen, *Adv. Space Res.* **35**, 1181–1184 (2005).
39. R. N. Manchester, D. P. Mar, A. G. Lyne, V. M. Kaspi, S. Johnston, *Astrophys. J.* **403**, L29 (1993).
40. R. P. Mignani *et al*., *Astron. Astrophys.* **515**, A110 (2010).
41. R. P. Mignani *et al*., *Astron. Astrophys.* **544**, A100 (2012).

ACKNOWLEDGMENTS

The Fermi-LAT Collaboration acknowledges support for LAT development, operation, and data analysis from NASA and the U.S. Department of Energy (DOE) (United States); Commissariat à l'Énergie Atomique (CEA)–Institut de Recherche sur les lois Fondamentales de l'Univers (IRFU) and Institut National de Physique Nucléaire et de Physique des Particules/Centre National de la Recherche Scientifique (France); Agenzia Spaziale Italiana (ASI) and Istituto Nazionale di Fisica Nucleare (Italy); Ministry of Education, Culture, Sports, Science and Technology, KEK, and Japan Aerospace Exploration Agency (Japan); and the K. A. Wallenberg Foundation, the Swedish Research Council, and the National Space Board (Sweden). Science analysis support in the operations phase from the Istituto Nazionale di Astrofisica (INAF) (Italy) and Centre National d'Études Spatiales (France) is also gratefully acknowledged. Fermi-LAT data and analysis tools are publicly available from the Fermi Science Support Center at http://fermi.gsfc.nasa.gov/ssc. M.R. was funded by contract FIRB-2012-RBFR12PM1F from the Italian Ministry of Education, University and Research (MIUR).

M. Ackermann,[1] A. Albert,[2] L. Baldini,[2,3] J. Ballet,[4] G. Barbiellini,[5,6] C. Barbieri,[7] D. Bastieri,[8,9] R. Bellazzini,[10] E. Bissaldi,[11] R. Bonino,[12,13] E. Bottacini,[2] T. J. Brandt,[14] J. Bregeon,[15] P. Bruel,[16] R. Buehler,[1] G. A. Caliandro,[2,17] R. A. Cameron,[2] P. A. Caraveo,[18] C. Cecchi,[19,20] E. Charles,[2] A. Chekhtman,[21] C. C. Cheung,[22] J. Chiang,[2] G. Chiaro,[9] S. Ciprini,[19,23,24] J. Cohen-Tanugi,[15] A. Cuoco,[12,13] S. Cutini,[19,23,24] F. D'Ammando,[25,26] F. de Palma[11,27] R. Desiante,[5,28] S. W. Digel,[2] L. Di Venere,[29] P. S. Drell,[2] C. Favuzzi,[11,29] S. J. Fegan,[16] E. C. Ferrara,[14] A. Franckowiak,[2] S. Funk,[30] P. Fusco,[11,29] F. Gargano,[11] D. Gasparrini,[19,23,24] N. Giglietto,[11,29] F. Giordano,[11,29] G. Godfrey,[2] I. A. Grenier,[4] M.-H. Grondin,[31] J. E. Grove,[22] L. Guillemot,[32,33] S. Guiriec,[14,34] K. Hagiwara,[35] A. K. Harding,[14] E. Hays,[14] J. W. Hewitt,[36,37] A. B. Hill,[2,38] D. Horan,[16] T. J. Johnson,[21] J. Knödlseder,[39,40] M. Kuss,[10] S. Larsson,[41,42] L. Latronico,[12] M. Lemoine-Goumard,[31] J. Li,[43] L. Li,[41,42] F. Longo,[5,6] F. Loparco,[11,29] M. N. Lovellette,[22] P. Lubrano,[19,20] S. Maldera,[12] A. Manfreda,[10] F. Marshall,[14] P. Martin,[39,40] M. Mayer,[1] M. N. Mazziotta,[11] P. F. Michelson,[2] N. Mirabal,[14,34] T. Mizuno,[44] M. E. Monzani,[2] A. Morselli,[45] I. V. Moskalenko,[2] S. Murgia,[46] G. Naletto,[47,48] E. Nuss,[15] T. Ohsugi,[44] M. Orienti,[25] E. Orlando,[2] D. Paneque,[2,49] M. Pesce-Rollins,[2,10] F. Piron,[15] G. Pivato,[10] T. A. Porter,[2] S. Rainò,[11,29] R. Rando,[8,9] M. Razzano,[10] A. Reimer,[2,50] O. Reimer,[2,50] T. Reposeur,[31] R. W. Romani,[2] P. M. Saz Parkinson,[51,52] A. Schulz,[1] C. Sgrò,[10] E. J. Siskind,[53] D. A. Smith,[31] F. Spada,[10] G. Spandre,[10] P. Spinelli,[11,29] D. J. Suson,[54] H. Takahashi,[55] J. B. Thayer,[2] D. J. Thompson,[14] L. Tibaldo,[2] D. F. Torres,[43,56] Y. Uchiyama,[35] G. Vianello,[2] K. S. Wood,[22] M. Wood,[2] L. Zampieri[58]

[1]Deutsches Elektronen Synchrotron DESY, D-15738 Zeuthen, Germany. [2]W. W. Hansen Experimental Physics Laboratory, Kavli Institute for Particle Astrophysics and Cosmology, Department of Physics and SLAC National Accelerator Laboratory, Stanford

University, Stanford, CA 94305, USA. [3]Università di Pisa and Istituto Nazionale di Fisica Nucleare, Sezione di Pisa I-56127 Pisa, Italy. [4]Laboratoire Astrophysique Interactions Multi-échelles, CEA-IRFU/CNRS/Université Paris Diderot, Service d'Astrophysique, CEA Saclay, F-91191 Gif sur Yvette, France. [5]Istituto Nazionale di Fisica Nucleare, Sezione di Trieste, I-34127 Trieste, Italy. [6]Dipartimento di Fisica, Università di Trieste, I-34127 Trieste, Italy. [7]Department of Physics and Astronomy, University of Padova, Vicolo Osservatorio 3, I-35122 Padova, Italy. [8]Istituto Nazionale di Fisica Nucleare, Sezione di Padova, I-35131 Padova, Italy. [9]Dipartimento di Fisica e Astronomia "G. Galilei", Università di Padova, I-35131 Padova, Italy. [10]Istituto Nazionale di Fisica Nucleare, Sezione di Pisa, I-56127 Pisa, Italy. [11]Istituto Nazionale di Fisica Nucleare, Sezione di Bari, I-70126 Bari, Italy. [12]Istituto Nazionale di Fisica Nucleare, Sezione di Torino, I-10125 Torino, Italy. [13]Dipartimento di Fisica Generale "Amadeo Avogadro," Università degli Studi di Torino, I-10125 Torino, Italy. [14]NASA Goddard Space Flight Center, Greenbelt, MD 20771, USA. [15]Laboratoire Univers et Particules de Montpellier, Université Montpellier, CNRS/IN2P3, Montpellier, France. [16]Laboratoire Leprince-Ringuet, École polytechnique, CNRS/IN2P3, Palaiseau, France. [17]Consorzio Interuniversitario per la Fisica Spaziale, I-10133 Torino, Italy. [18]INAF-Istituto di Astrofisica Spaziale e Fisica Cosmica, I-20133 Milano, Italy. [19]Istituto Nazionale di Fisica Nucleare, Sezione di Perugia, I-06123 Perugia, Italy. [20]Dipartimento di Fisica, Università degli Studi di Perugia, I-06123 Perugia, Italy. [21]College of Science, George Mason University, Fairfax, VA 22030, resident at Naval Research Laboratory, Washington, DC 20375, USA. [22]Space Science Division, Naval Research Laboratory, Washington, DC 20375-5352, USA. [23]Agenzia Spaziale Italiana (ASI) Science Data Center, I-00133 Roma, Italy. [24]INAF Osservatorio Astronomico di Roma, I-00040 Monte Porzio Catone (Roma), Italy. [25]INAF Istituto di Radioastronomia, I-40129 Bologna, Italy. [26]Dipartimento di Astronomia, Università di Bologna, I-40127 Bologna, Italy. [27]Università Telematica Pegaso, Piazza Trieste e Trento, 48, I-80132 Napoli, Italy. [28]Università di Udine, I-33100 Udine, Italy. [29]Dipartimento di Fisica "M. Merlin" dell'Università e del Politecnico di Bari, I-70126 Bari, Italy. [30]Erlangen Centre for Astroparticle Physics, D-91058 Erlangen, Germany. [31]Centre d'Études Nucléaires de Bordeaux Gradignan, IN2P3/CNRS, Université Bordeaux 1, BP120, F-33175 Gradignan Cedex, France. [32]Laboratoire de Physique et Chimie de l'Environnement et de l'Espace–Université d'Orléans/CNRS, F-45071 Orléans Cedex 02, France. [33]Station de Radioastronomie de Nançay, Observatoire de Paris, CNRS/INSU, F-18330 Nançay, France. [34]NASA Postdoctoral Program Fellow, USA. [35]3-34-1 Nishi-Ikebukuro, Toshima-ku, Tokyo 171-8501, Japan. [36]Department of Physics and Center for Space Sciences and Technology, University of Maryland Baltimore County, Baltimore, MD 21250, USA. [37]Center for Research and Exploration in Space Science and Technology and NASA Goddard Space Flight Center, Greenbelt, MD 20771, USA. [38]School of Physics and Astronomy, University of Southampton, Highfield, Southampton, SO17 1BJ, UK. [39]CNRS, Institut de Recherche en Astrophysique et Planétologie (IRAP), F-31028 Toulouse cedex 4, France. [40]Université de Toulouse, Université Toulouse III–Paul Sabatier–Observatoire Midi-Pyrénées, IRAP, Toulouse, France. [41]Department of Physics, KTH Royal Institute of Technology, AlbaNova, SE-106 91 Stockholm, Sweden. [42]The Oskar Klein Centre for Cosmoparticle Physics, AlbaNova, SE-106 91 Stockholm, Sweden. [43]Institute of Space Sciences (Institut d'Estudis Espacials de Catalunya–Consejo Superior de Investigaciones Científicas), Campus UAB, E-08193 Barcelona, Spain. [44]Hiroshima Astrophysical Science Center, Hiroshima University, Higashi-Hiroshima, Hiroshima 739-8526, Japan. [45]Istituto Nazionale di Fisica Nucleare, Sezione di Roma "Tor Vergata," I-00133 Roma, Italy. [46]Center for Cosmology, Physics and Astronomy Department, University of California, Irvine, CA 92697-2575, USA. [47]Consiglio Nazionale delle Ricerche–Istituto Di Fotonica E Nanotecnologie UOS Padova LUXOR, via Trasea 7, I-35131 Padova, Italy. [48]Department of Information Engineering, University of Padova, Via G. Gradenigo 6/B, I-35131 Padova, Italy. [49]Max-Planck-Institut für Physik, D-80805 München, Germany. [50]Institut für Astro- und Teilchenphysik and Institut für Theoretische Physik, Leopold-Franzens-Universität Innsbruck, A-6020 Innsbruck, Austria. [51]Santa Cruz Institute for Particle Physics, Department of Physics and Department of Astronomy and Astrophysics, University of California at Santa Cruz, Santa Cruz, CA 95064, USA. [52]Department of Physics, The University of Hong Kong, Pokfulam Road, Hong Kong, China. [53]NYCB Real-Time Computing, Lattingtown, NY 11560-1025, USA. [54]Department of Chemistry and Physics, Purdue University Calumet, Hammond, IN 46323-2094, USA. [55]Department of Physical Sciences, Hiroshima University, Higashi-Hiroshima, Hiroshima 739-8526, Japan. [56]Institució Catalana de Recerca i Estudis Avançats, Barcelona, Spain. [57]INAF–Astronomical Observatory of Padova, Vicolo dell'Osservatorio 5, I-35122 Padova, Italy.

SUPPLEMENTARY MATERIALS

www.sciencemag.org/content/350/6262/801/suppl/DC1
Materials and Methods
Fig. S1
Tables S1 and S2
References (*42*, *43*)

5 June 2015; accepted 7 October 2015
10.1126/science.aac7400

MAMMALIAN EVOLUTION

Evolution and dispersal of mammoths across the Northern Hemisphere

A. M. Lister[1]* and A. V. Sher[2]†

Mammoths provide a detailed example of species origins and dispersal, but understanding has been impeded by taxonomic confusion, especially in North America. The Columbian mammoth *Mammuthus columbi* was thought to have evolved in North America from a more primitive Eurasian immigrant. The earliest American mammoths (1.5 million years ago), however, resemble the advanced Eurasian *M. trogontherii* that crossed the Bering land bridge around that time, giving rise directly to *M. columbi*. Woolly mammoth *M. primigenius* later evolved in Beringia and spread into Europe and North America, leading to a diversity of morphologies as it encountered endemic *M. trogontherii* and *M. columbi*, respectively. In North America, this included intermediates ("*M. jeffersonii*"), suggesting introgression of *M. primigenius* with *M. columbi*. The lineage illustrates the dynamic interplay of local adaptation, dispersal, and gene flow in the evolution of a widely distributed species complex.

Mammoths arrived in Eurasia from Africa around 3 million years ago (Ma) and underwent remarkable adaptive evolution through species *Mammuthus meridionalis* and *M. trogontherii* to *M. primigenius* (the woolly mammoth), with changes in molar and skull structure adaptive to grazing in the increasingly open habitats of the Pleistocene (*1*). Although the pattern is well documented for Eurasia, our understanding of the origin and evolution of North American mammoths is much less clear (Fig. 1).

Our study focused on upper and lower last molars (M^3 and M_3), which show most clearly the lineage transformations (Fig. 2) (*2*). In Europe, the average number of enamel lamellae increases from 13 (*M. meridionalis*) to 19 (*M. trogontherii*) to 24 (*M. primigenius*), while hypsodonty (crown height) almost doubles between the first two species, which also show the most profound changes in skull morphology (*3*–*5*).

The earliest mammoths in North America, and hence their likely time of arrival, date to ~ 1.5 to 1.3 Ma (*6*, *7*). The prevailing view is that early American mammoths were of "primitive" morphology, indicating a close relationship to *M. meridionalis*, the contemporary species in Europe. Early North American fossils have been referred either to that form or to the supposedly related *M. hayi* or *M. haroldcooki* (*8*–*13*). From here, an evolutionary sequence is posited, leading to the late Pleistocene Columbian mammoth *M. columbi*. The transformations would have paralleled those from *M. meridionalis* to *M. trogontherii* in Eurasia, and the species *M. imperator* is frequently cited as an "intermediate" stage (*10*, *14*) (Fig. 1A).

We focused on dated samples but included undated North American specimens that have been referred to "primitive" taxa such as *M. meridionalis* and *M. hayi* (*2*). We found no specimen comparable to Eurasian *M. meridionalis*. Past identifications were often based on worn molars and failed to take into account the mode of eruption and wear among elephants (*2*). Molars replace each other from behind and move slowly forward through the jaw, suffering anterior attrition as they reach the front, progressively reducing molar length and number of lamellae and giving an artificially primitive appearance (Fig. 3). We used the configuration of the anterior roots (*15*), plus the crown length/width ratio expected from complete teeth, to recognize anterior loss, and found that all supposedly primitive molars with 11 to 15 lamellae were incomplete, and the original count was higher or unknown (Fig. 3, supplementary text, and data sets S1 and S2). Conversely, where early and middle Pleistocene molars are complete, they invariably show lamellar counts of 18 to 21, like typical *M. columbi* (Figs. 2C and 4, B and D; figs. S33 and S35 to S40; and data sets S1 and S2). In crown height, the most critical evolutionary index in the lineage, all measurable

[1]Department of Earth Sciences, Natural History Museum, London SW7 5BD, UK. [2]Severtsov Institute of Ecology and Evolution, Moscow 119071, Russia.
***Corresponding author. E-mail: a.lister@nhm.ac.uk** †Deceased.

An extremely bright gamma-ray pulsar in the Large Magellanic Cloud

The Fermi LAT Collaboration

Science **350** (6262), 801-805.
DOI: 10.1126/science.aac7400

LMC pulsar's bright gamma-ray flashes

Pulsars are rapidly rotating neutron stars that are seen as pulsating sources of radio waves. Some, such as the Crab pulsar, also emit pulses of gamma rays. The Fermi LAT collaboration observed pulsed gamma rays from a pulsar outside our galaxy, the Milky Way. The pulsar, known as PSR J0540–6919, is located in the Large Magellanic Cloud (LMC). This is the most powerful gamma-ray pulsar yet known, with luminosity 20 times that of the Crab. The findings should help to explain how pulsars convert the energy stored in their rotation into detectable electromagnetic emission.

Science, this issue p. 801